Acta Crystallographica Section D
Biological Crystallography
ISSN 0907-4449

Structures of human sirtuin 3 complexes with ADP-ribose and with carba-NAD$^+$ and SRT1720: binding details and inhibition mechanism

Giang Thi Tuyet Nguyen, Susanne Schaefer, Melanie Gertz, Michael Weyand* and Clemens Steegborn*

Department of Biochemistry, University of Bayreuth, Universitätsstrasse 30, 95445 Bayreuth, Germany

Correspondence e-mail: michael.weyand@uni-bayreuth.de, clemens.steegborn@uni-bayreuth.de

Received 9 May 2013
Accepted 3 June 2013

PDB References: Sirt3–ADP-ribose, 4bn4; Sirt3–carba-NAD$^+$–SRT1720, 4bn5

Sirtuins are NAD$^+$-dependent protein deacetylases that regulate metabolism and aging processes and are considered to be attractive therapeutic targets. Most available sirtuin modulators are little understood mechanistically, hindering their improvement. SRT1720 was initially described as an activator of human Sirt1, but it also potently inhibits human Sirt3. Here, the molecular mechanism of the inhibition of Sirt3 by SRT1720 is described. A crystal structure of Sirt3 in complex with SRT1720 and an NAD$^+$ analogue reveals that the compound partially occupies the acetyl-Lys binding site, thus explaining the reported competition with the peptide substrate. The compound packs against a hydrophobic protein patch and binds with its opposite surface to the NAD$^+$ nicotinamide, resulting in an exceptionally tight sandwich-like interaction. The observed arrangement rationalizes the uncompetitive inhibition with NAD$^+$, and binding measurements confirm that the nicotinamide moiety of NAD$^+$ supports inhibitor binding. Consistently, no inhibitor is bound in a second crystal structure of Sirt3 that was solved complexed with ADP-ribose and crystallized in the presence of SRT1720. These results reveal a novel sirtuin inhibitor binding site and mechanism, and provide a structural basis for compound improvement.

1. Introduction

Sirtuins are conserved NAD$^+$-dependent protein deacetylases. The seven mammalian sirtuin isoforms (Sirt1–7) regulate, for example, energy metabolism and stress responses by modifying specific substrate proteins in different cellular compartments (Michan & Sinclair, 2007; Haigis & Sinclair, 2010). Sirt1, Sirt6 and Sirt7 are nuclear, and regulate transcription factors and DNA homeostasis, while cytosolic Sirt2 deacetylates, for example, tubulin (North *et al.*, 2003). Sirt3, Sirt4 and Sirt5 are mitochondrial isoforms and regulate various metabolic enzymes (Verdin *et al.*, 2010; Gertz & Steegborn, 2010; Laurent *et al.*, 2013). Owing to these physiological functions, sirtuins are considered to be attractive therapeutic targets for diseases such as metabolic disorders and cancer (Lavu *et al.*, 2008; Haigis & Sinclair, 2010).

Sirtuins contain a conserved catalytic core domain with distinct N-terminal and C-terminal extensions (Michan & Sinclair, 2007). The two substrates, acetyl-Lys polypeptide and NAD$^+$, bind at a cleft between two subdomains: a smaller zinc-binding domain and a larger Rossmann-fold domain. During catalysis, the nicotinamide (NAM) moiety of NAD$^+$ is inserted in the so-called C-site and the carbonyl O atom of the acetyl-Lys attacks the strained C1′ position of the connected ribose,

resulting in the release of NAM and the formation of an alkylimidate intermediate (Sauve *et al.*, 2006). Hydrolysis of the intermediate leads to the products deacetylated protein and 2′-*O*-acetylated ADP-ribose (Sauve *et al.*, 2006). Catalysis of some sirtuins can be activated by resveratrol and other small molecules identified in a high-throughput screen, such as *N*-{2-[3-(piperazin-1-ylmethyl)imidazo[2,1-*b*][1,3]thiazol-6-yl]-phenyl}quinoxaline-2-carboxamide (SRT1720; Fig. 1*a*), which appears to induce beneficial health effects and to mimic the life-span extension effect of caloric restriction in lower organisms (Minor *et al.*, 2010; Milne *et al.*, 2007). Development of improved sirtuin activators is of great interest, but although several studies have confirmed and further characterized sirtuin activation, it is mechanistically not fully understood (Gertz *et al.*, 2012; Lakshminarasimhan, Rauh *et al.*, 2013; Hubbard *et al.*, 2013). Even more compounds have been described for sirtuin inhibition, such as cambinol, Ex-527 and salermide (Cen, 2010; Chen, 2011). Many of these compounds show limited isoform specificity and/or potency, however, and their inhibition mechanisms have mostly not been characterized, severely hindering further inhibitor improvement. Interestingly, the human Sirt1 (hSirt1) activators resveratrol and SRT1720 were found to inhibit rather than activate Sirt3, an isoform for which no potent and selective compounds are currently available. Competition studies using activity assays indicated that SRT1720 acts competitively with the substrate peptide and uncompetitively with NAD^+ (Jin, Galonek *et al.*, 2009), but details of the binding site and inhibition mechanism of the compound remain to be revealed.

Here, we describe biochemical and crystal structure analyses revealing the mechanism of inhibition of Sirt3 by SRT1720. The crystal structure of an hSirt3 complex with an NAD^+ analogue and SRT1720 reveals the compound-binding site, which is partially formed by the co-substrate NAD^+, and binding data confirm that the nicotinamide group of NAD^+ supports inhibitor binding. The structure rationalizes the reported uncompetitive inhibition pattern with NAD^+, and its analysis indicates approaches for further inhibitor improvements.

2. Materials and methods

2.1. Chemicals, peptides and hSirt1 protein

Chemicals were from Sigma (St Louis, USA) if not stated otherwise. SRT1720 was from Cayman Chemical (Ann Arbor, USA). HPLC-purified ACS2 peptide [TRSG(acetylK)-VMRRL] was from GL Biochem (Shanghai, People's Republic of China) and FdL-1 peptide was from Enzo Life Sciences (Farmingdale, USA). hSirt1 protein was purified as described by Schlicker *et al.* (2011). In brief, full-length hSirt1 with an N-terminal His tag was expressed in *Escherichia coli* BL21(DE3) Rosetta2 cells (Merck, Germany) and purified by affinity chromatography with TALON resin followed by gel-filtration chromatography in 25 m*M* HEPES pH 7.5, 100 m*M* KCl, 2 m*M* DTT.

2.2. Preparation of hSirt3 protein and crystallization of hSirt3 complexes

hSirt3 protein (residues 118–399; UniProt entry Q9NTG7) was expressed in *E. coli* BL21(DE3) Rosetta2 cells and purified as described previously (Gertz *et al.*, 2012). In brief, the protein was expressed as a His-Trx fusion and purified by TALON affinity chromatography; the tag was then cleaved using *Tobacco etch virus* (TEV) protease. The tag was removed by additional TALON chromatography followed by size-exclusion chromatography in 20 m*M* Tris–HCl pH 7.8, 150 m*M* NaCl.

Crystallization was performed with a semi-automated Phoenix nanolitre pipetting robot (ARI Robotics Ltd) using commercially available JCSG Core Suite screens (Qiagen, Hilden, Germany). For setting up screens, we used a protein sample at a concentration of 10 mg ml^{-1} mixed with 5 m*M* carba-NAD^+ and 2 m*M* SRT1720 in the presence of 10%(*v*/*v*) DMSO (hSirt3–carba-NAD^+–SRT1720 complex) or with 2 m*M* NAD^+, 1 m*M* SRT1720 in the presence of 5%(*v*/*v*) DMSO (hSirt3–ADP-ribose complex). Crystals of the hSirt3–carba-NAD^+–SRT1720 complex were identified in a condition consisting of 20%(*w*/*v*) PEG 3350, 0.2 *M* sodium fluoride (JCSG Core II Suite condition No. 29); crystals of the hSirt3–ADP-ribose complex were identified in a condition consisting of 30%(*v*/*v*) PEG 600, 5%(*w*/*v*) PEG 1000, 10%(*v*/*v*) glycerol, 0.1 *M* MES buffer pH 6.0 (JCSG Core IV Suite condition No. 71). In both cases, X-ray data collection was performed on protein crystals directly harvested from the screening plate.

2.3. Diffraction data collection, structure determination and refinement

hSirt3 crystals were cryoprotected in mother liquor supplemented with 20%(*v*/*v*) glycerol and cooled in liquid nitrogen. Complete diffraction data sets were collected from single crystals at 100 K on beamline 14.1 operated by the Helmholtz-Zentrum Berlin (HZB) at the BESSY II electron-storage ring (Berlin, Germany; Mueller *et al.*, 2012). For the hSirt3–carba-NAD^+–SRT1720 complex, data were collected at a wavelength of 0.91841 Å with a PILATUS 6M detector and with 0.1° oscillation per frame. For the hSirt3–ADP-ribose complex, data were collected at a wavelength of 0.91841 Å with a MAR CCD detector and with 1.0° oscillation per frame. Indexing and data reduction were performed with *XDS* (Kabsch, 2010), with high-resolution cutoffs chosen based on the CC* criterion (Karplus & Diederichs, 2012) as implemented in *XDS*.

The structure of the hSirt3–carba-NAD^+–SRT1720 complex was solved by molecular replacement (MR) with *Phaser* using one monomer of the apo Sirt3 structure (PDB entry 3gls; Jin, Wei *et al.*, 2009) without coordinates for the cofactor-binding loop atoms as a search model. The asymmetric unit contains 12 chains, with a solvent content of 72.1% and a Matthews coefficient of 4.41 Å^3 Da^{-1}. The initial model was refined by several rounds of manual rebuilding with *Coot* (Emsley & Cowtan, 2004) and refinement with *REFMAC* (Murshudov *et al.*, 2011). The *REFMAC* TLS option (with each of the 12

complexes in the asymmetric unit treated as one TLS group) and local auto NCS restraints (Murshudov *et al.*, 2011) were used throughout refinement. *B* factors were fixed at 20 Å^2 for protein atoms and were only refined for nonprotein atoms (SRT1720 and Zn^{2+} ions), and overall TLS contributions were added to the coordinate file during the last refinement cycle. The electron density for the Zn^{2+} ion in several molecules was not well defined, a phenomenon that was also observed in some other sirtuin crystal structures and that is thus not likely to be a consequence of the low resolution. Parameter files for SRT1720 were obtained using *PRODRG* (Schüttelkopf & van Aalten, 2004), which was also used to obtain parameter files for carba-NAD$^+$ since the parameters from the PDB contained a mistake in the cyclopentane ring. The high-resolution structure of the hSirt3–ADP-ribose complex was also solved by MR using the same apo Sirt3 structure as the search model. Model building and incorporation of 266 water molecules were performed with the automatic model-building options within *Coot*. Anisotropic restrained *B* factors were refined with *REFMAC*. For both structures, structure-factor amplitudes were used as refinement targets and all measured reflections were used during refinement, split into a working set (95%) and test set (5%). van der Waals distances were not restrained during refinement. The final data-processing and refinement statistics are given in Table 1.

The refined structures were evaluated using *Coot*, *MolProbity* and *PROCHECK* (Emsley & Cowtan, 2004; Chen *et al.*, 2010; Laskowski *et al.*, 1993), and real-space correlation coefficients were calculated with *MAPMAN* (Kleywegt, 1999). In the hSirt3–carba-NAD$^+$–SRT1720 model, 84.7% of the protein residues were in the most favoured regions of the Ramachandran plot, 14.3% were in additional allowed regions, 0.9% were in generously allowed regions and 0.1% were in

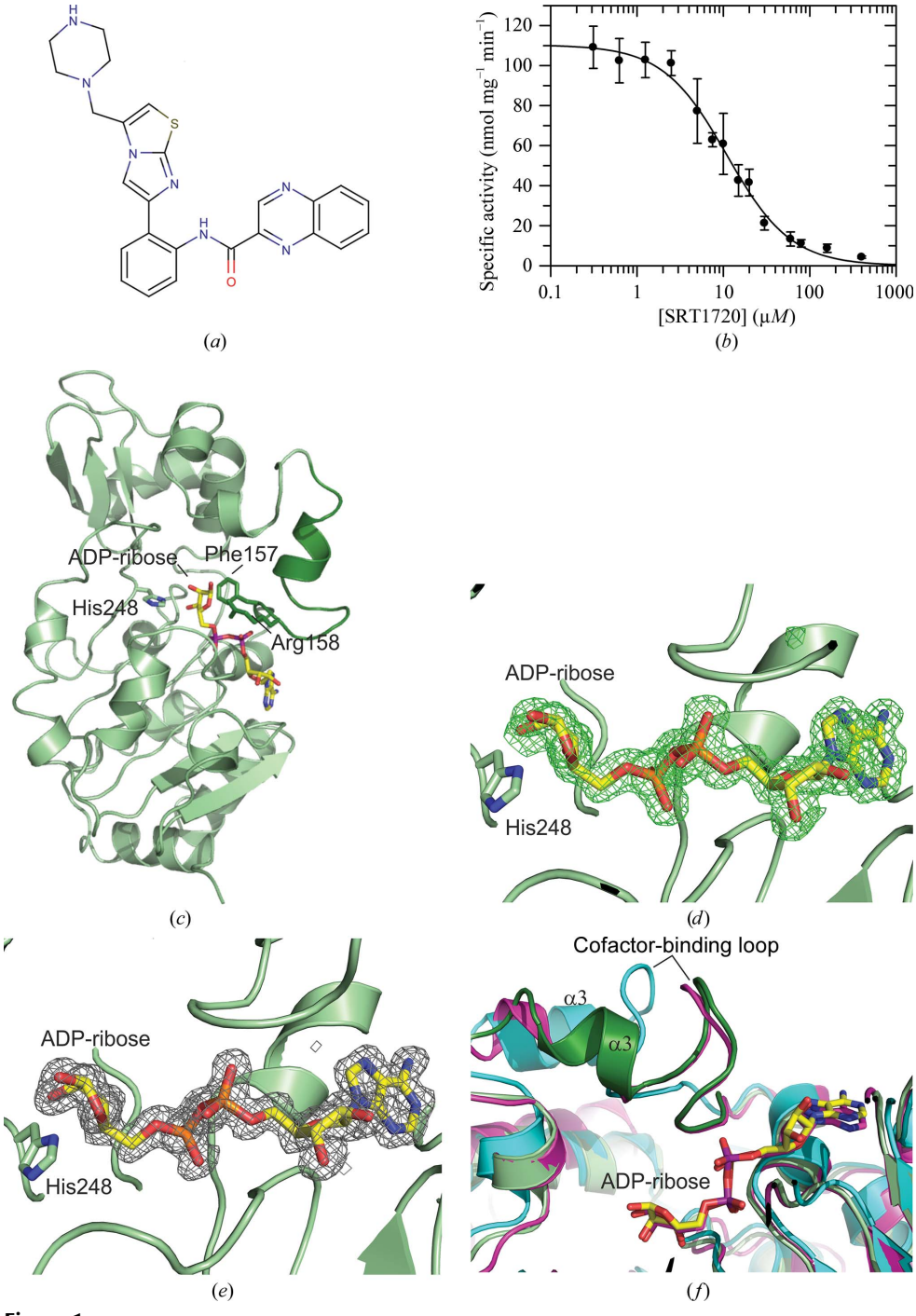

Figure 1
hSirt3 inhibition by SRT1720 and the crystal structure of an hSirt3–ADP-ribose complex. (*a*) Chemical structure of SRT1720 (*N*-{2-[3-(piperazin-1-ylmethyl)imidazo[2,1-*b*][1,3]thiazol-6-yl]phenyl}quinoxaline-2-carboxamide). (*b*) IC_{50} determination for SRT1720 against hSirt3 using a mass-spectrometry-based activity assay with 500 μ*M* ACS2 peptide and 2.5 m*M* NAD^+ as substrates. Error bars represent standard errors of linear fits to time-series experiments. (*c*) Overall crystal structure of hSirt3 in complex with ADP-ribose (yellow). The cofactor-binding loop, which can assume different conformations depending on the bound ligands, is shown in dark green. (*d*) Detailed view of the active site of the hSirt3–ADP-ribose complex with $F_o - F_c$ OMIT density for the ligand contoured at 3.0σ. (*e*) Active site of the hSirt3–ADP-ribose complex with ligand $2F_o - F_c$ density contoured at 1.0σ. (*f*) Comparison of the cofactor-binding loop regions of the ADP-ribose complexes of hSirt3 (green) and hSirt2 (magenta; PDB entry 3zgv; Moniot *et al.*, 2013) and of the hSirt3 apo form (cyan; PDB entry 3gls; Jin, Wei *et al.*, 2009).

Table 1
Diffraction data and refinement statistics.

Values in parentheses are for the outermost shell.

	Sirt3–ADP-ribose	Sirt3–carba-NAD$^+$–SRT1720
Data processing		
Space group	$P2_12_12_1$	$C2$
Unit-cell parameters (Å, °)	a = 63.9, b = 66.7, c = 66.9, β = 90.0	a = 227.8, b = 246.1, c = 127.3, β = 123.9
Resolution (Å)	47.2–1.3 (1.40–1.30)	45.8–3.25 (3.30–3.25)
Unique reflections	69702 (13500)	91148 (4092)
Observations	474454 (55816)	352538 (15908)
Completeness (%)	98.4 (96.8)	99.4 (99.6)
Multiplicity	6.8 (4.1)	3.9 (3.9)
R_{meas}† (%)	8.8 (136.2)	14.4 (144.0)
$\langle I/\sigma(I)\rangle$	15.1 (1.2)	9.3 (1.1)
Refinement		
Protein chains in asymmetric unit	1	12
Solvent content (%)	51.7	72.1
No. of amino acids	272	3275
No. of protein atoms	2489	25548
No. of ligand atoms	41	936
No. of waters	266	0
No. of solvent atoms (except water)	20	24
No. of metals	2	12
Resolution (Å)	47.2–1.30 (1.334–1.300)	45.8–3.25 (3.334–3.250)
R_{cryst}‡/R_{free}§ (%)	13.8/17.9 (28.7/32.6)	22.7/24.7 (38.5/41.1)
B factors (Å^2)		
Protein	20.4	20.0 (fixed)¶
Ligands (including metals)	15.0	86.2¶
Water	37.9	—
Solvent atoms	46.3	86.2
R.m.s.d. bond lengths/target (Å)	0.023/0.019	0.018/0.020
R.m.s.d. angles/target (°)	2.319/2.012	2.381/2.031
R.m.s.d. planes/target (Å)	0.013/0.020	0.010/0.021

† $R_{meas} = \sum_{hkl}\{N(hkl)/[N(hkl)-1]\}^{1/2}\sum_i |I_i(hkl) - \langle I(hkl)\rangle|/\sum_{hkl}\sum_i I_i(hkl)$. ‡ $R_{cryst} = \sum_{hkl}||F_{obs}| - |F_{calc}||/\sum_{hkl}|F_{obs}|$, where $|F_{obs}|$ is the observed and $|F_{calc}|$ is the calculated structure-factor amplitude. § R_{free} was calculated from 5% of measured reflections that were omitted from refinement. ¶ Protein-atom B factors were not refined; TLS contributions were added to the deposited coordinate file in the final *REFMAC* refinement cycle.

disallowed regions. In the hSirt3–ADP-ribose model, 91.7% of the residues were in the most favoured regions of the Ramachandran plot and 8.3% were in additional allowed regions; no residues were in generously allowed or disallowed regions. Structure figures were generated with *PyMOL* (http://www.pymol.org) and the schematic view of the interactions with *LIGPLOT* (Wallace *et al.*, 1995). For generating OMIT maps for ligands, the ligand was removed, the coordinates were randomized by 0.24 Å with *MOLEMAN*2 (Kleywegt, 2000) and the ligand-free and randomized structure was refined in *REFMAC*.

2.4. Deacetylation, binding and thermal denaturation assays

A commercial deacetylation kit was used for deacetylation assays with p53-derived fluorophore-labelled FdL-1 substrate peptide (Enzo Life Sciences). 1.5 µg of each protein was incubated with 0.1 m*M* FdL-1 and 1 m*M* NAD$^+$ in the presence of 20 µ*M* SRT1720 and 2%(*v*/*v*) DMSO, or with 2%(*v*/*v*) DMSO without compound as a control, for 30 min at 310 K. Samples were then incubated with developer for 45 min at room temperature and fluorescence was measured in a plate reader (excitation at 360 nm and emission at 460 nm). For deacetylation assays with ACS2-peptide, 10 µ*M* hSirt3 was incubated at 310 K with 0.5 m*M* ACS2 peptide and 2.5 m*M* NAD$^+$ in the presence or absence of the indicated SRT1720 concentrations. Control and all inhibition samples contained 2%(*v*/*v*) DMSO. Reactions were stopped after different time points by adding 0.25%(*v*/*v*) trifluoroacetic acid and were subjected to nano-LC-ESI-MS/MS analysis for quantification as described previously (Fischer *et al.*, 2012). Deacetylation activities were determined by linear fitting of time-series experiments. The K_i value was calculated using the equation given by Cheng & Prusoff (1973) for competitive inhibition, with peptide as competitive substrate, since the concentration used for NAD$^+$ in the relevant assays (2.5 m*M*) leads to almost complete saturation with this substrate, which shows uncompetitive behaviour (*i.e.* supports inhibitor binding).

To measure binding affinities, microscale thermophoresis (Wienken *et al.*, 2010) was analyzed using a NanoTemper Monolith NT.label-free instrument (25% UV-LED; 20–80% IR-laser power; NanoTemper Technologies, Germany). Samples contained 1 µ*M* hSirt3 in 20 m*M* Tris pH 7.8, 150 m*M* NaCl, 10%(*v*/*v*) DMSO and the indicated amounts of ligands (ADP-ribose, NAD$^+$ and SRT1720), and measurements were performed in duplicate. Binding transitions were fitted with a single-site equation in *Prism* (GraphPad Software, California, USA).

For thermal denaturation shift assays, hSirt3 in gel-filtration buffer was supplemented with 50 µ*M* SRT1720 [20 m*M* stock in DMSO; final DMSO concentration adjusted to 2%(*v*/*v*)], or DMSO as a control, in a 96-well PCR plate. After adding SYPRO Orange fluorescent dye and adding a layer of mineral oil to prevent evaporation, thermal denaturation was analyzed in an FluoDia fluorescence plate reader (PTI; Birmingham, USA), with excitation and emission wavelengths of 480 and 530 nm, respectively. Fluorescence data were fitted with a two-state transition equation to determine transition midpoints.

3. Results

3.1. Crystal structure of hSirt3 in complex with ADP-ribose

To confirm the inhibition of hSirt3 by SRT1720, we tested increasing compound concentrations in a mass-spectrometric assay with an acetyl-CoA synthetase 2 (ACS2)-derived substrate peptide. SRT1720 inhibited hSirt3 with an IC_{50} of 11 ± 1 µ*M* at 500 µ*M* peptide concentration (Fig. 1*b*), corresponding to a K_i of 0.62 µ*M* calculated according to Cheng & Prusoff (1973) (see §2.4) and based on the peptide competition

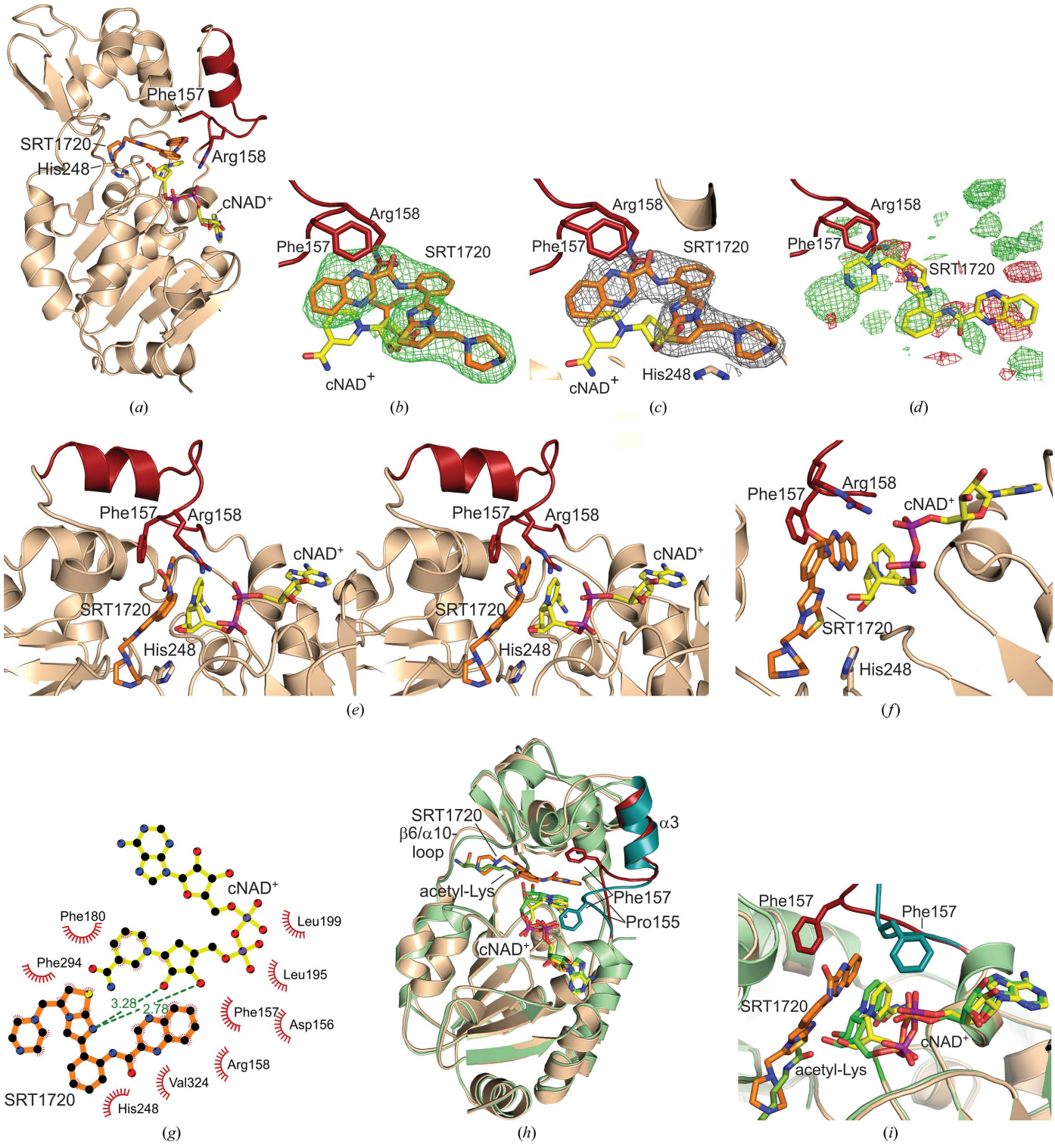

Figure 2
hSirt3 binding mode and inhibition mechanism of SRT1720. (*a*) Overall crystal structure of hSirt3 in complex with carba-NAD$^+$ (yellow) and SRT1720 (orange). (*b*) Active site of the hSirt3–carba-NAD$^+$–SRT1720 complex with $F_o - F_c$ OMIT density for the inhibitor contoured at 3.0σ. (*c*) hSirt3–carba-NAD$^+$–SRT1720 active site overlaid with $2F_o - F_c$ density for the inhibitor contoured at 1.0σ. (*d*) Active site of an hSirt3–carba-NAD$^+$–SRT1720 complex with the inhibitor refined in an alternative orientation and overlaid with the resulting $F_o - F_c$ difference density contoured at 3.0σ (green, positive density; red, negative density). (*e*) Stereoview of the active site and surroundings of the hSirt3–carba-NAD$^+$–SRT1720 complex. (*f*) Close-up view of the hSirt3–carba-NAD$^+$–SRT1720 active site. (*g*) Schematic view of the interactions between SRT1720, hSirt3 and carba-NAD$^+$. (*h*) Overlay of Sirt3 complexes with carba-NAD$^+$–SRT1720 (brown/yellow/orange) or ACS2-peptide–carba-NAD$^+$ (green; PDB entry 4fvt; Szczepankiewicz *et al.*, 2012) showing different cofactor-loop arrangements around Phe157 in the presence and absence of SRT1720. (*i*) Close-up view of the overlay of Sirt3 complexes with carba-NAD$^+$–SRT1720 (brown/yellow/orange) or ACS2-peptide–carba-NAD$^+$ (green; PDB entry 4fvt), showing a changed Phe157 orientation but a comparable carba-NAD$^+$ conformation upon inhibitor binding. Carba-NAD$^+$ is labelled cNAD$^+$.

reported previously (Jin, Galonek *et al.*, 2009; see also below), which fits well with the value reported in that study (0.56 μ*M*). To identify the hSirt3 binding site for SRT1720 and to reveal the inhibition mechanism of the compound, we then attempted to solve a crystal structure of hSirt3 in complex with SRT1720. Since SRT1720 appears to act uncompetitively with NAD^+ (Jin, Galonek *et al.*, 2009), *i.e.* NAD^+ seems to support compound binding, we included NAD^+ in the cocrystallization trials. hSirt3 crystals were obtained under various conditions and with different morphologies, but the respective structures showed the ADP-ribose moiety of NAD^+ to be the only ligand. We assume that the NAD^+ hydrolyzed during crystallization, consistent with the fact that some other sirtuin structures crystallized in the presence of NAD^+ also instead contained ADP-ribose (Chang *et al.*, 2002; Avalos *et al.*, 2004). We included one of the hSirt3–ADP-ribose structures, refined at 1.3 Å resolution, in this manuscript for comparative analyses (Fig. 1*c*; Table 1). The well defined ADP-ribose (Figs. 1*d* and 1*e*) occupies the NAD^+ site, and the so-called cofactor-binding loop (dark green in Fig. 1*c*) is layered on top of the ligand. This loop has been reported to undergo a ligand-induced binding-site closure movement (Moniot *et al.*, 2012; Sanders *et al.*, 2010), and comparison of our complex with an apo hSirt3 structure (Fig. 1*f*; Jin, Wei *et al.*, 2009) indeed shows that the pronounced loop interactions with ADP-ribose are enabled by a shift of the cofactor-binding loop and helix α3 towards the ligand. The 'closed' loop conformation places Phe157 next to the ribose (Fig. 1*c*), consistent with its proposed function to shield this position from solvent and against rebinding of nicotinamide released from NAD^+ during catalysis (Hoff *et al.*, 2006). In an hSirt2–ADP-ribose complex structure (Moniot *et al.*, 2013), the ligand and cofactor-binding loop assume almost identical conformations (Fig. 1*f*). This similarity supports the conclusion that the observed 'closed' loop conformation is not influenced by crystal packing and is consistent with the general sirtuin-isoform-independent functions of the cofactor-binding loop and Phe157.

3.2. Crystal structure of hSirt3 in complex with SRT1720 and carba-NAD^+

Since NAD^+ appears to show a tendency to hydrolyze during crystallization, we replaced it with the more stable analogue carba-NAD^+ (Szczepankiewicz *et al.*, 2012) in the crystallization setups, which indeed allowed us to solve a structure of hSirt3 with bound SRT1720 and co-substrate analogue at 3.25 Å resolution (Table 1). The overall structure of the ternary hSirt3–carba-NAD^+–SRT1720 complex (Fig. 2*a*) is comparable to other sirtuin–NAD^+ complexes except for the dynamic cofactor-binding loop (see below). SRT1720 could clearly be identified in the direct neighbourhood of the co-substrate analogue (Figs. 2*b* and 2*c*). The electron-density quality varied slightly between the 12 monomers in the asymmetric unit, but the inhibitor was clearly visible in identical positions in all monomers, with real-space correlation coefficients for SRT1720 of between 0.74 (monomer *A*; shown in our figures) and 0.91 (monomers *H* and *I*). Since rotation of the inhibitor from the orientation in our model (orientation I) by 180° around an axis perpendicular to the imidazole system of the compound would result in a roughly similar shape, we also refined a complex with this alternative orientation II. The $F_o - F_c$ difference density obtained for the alternative complex II (Fig. 2*d*) clearly documents the better fit of SRT1720 orientation I (Figs. 2*b* and 2*c*), in particular for the terminal piperazine and quinoxaline moieties. Comparison of real-space correlation coefficients supports this conclusion, since higher values were obtained for SRT1720 in orientation I in all 12 monomers (0.74 for orientation I *versus* 0.60 for orientation II in monomer *A*; the average for all monomers is 0.83 for orientation I and 0.70 for orientation II). We thus conclude that SRT1720 is bound in orientation I (Figs. 2*a*, 2*b* and 2*c*) in its complex with Sirt3–carba-NAD^+.

In the hSirt3–carba-NAD^+–SRT1720 complex (Figs. 2*e*, 2*f* and 2*g*), the inhibitor is positioned in the direct neighbourhood of the co-substrate analogue (Figs. 2*h* and 2*i*). The piperazine group and part of the connected imidazothiazole system of SRT1720 occupy the hydrophobic acetyl-Lys binding region (Figs. 2*e*, 2*h* and 2*i*), explaining the reported competition with substrate peptide (Jin, Galonek *et al.*, 2009). The imidazothiazole forms the only hydrogen bond of SRT1720 to carba-NAD^+, between the thiazole N atom and the NAM ribose 2′-hydroxyl group of the co-substrate analogue. The central phenyl moiety of SRT1720 is layered upon this carba-NAD^+ ribose and points with its edge out of the Sirt3 active site into the solvent. The quinoxaline ring of the inhibitor, in contrast, is oriented, through the carboxamide linker, back into the active site of the Sirt3–co-substrate analogue complex and is deeply buried. It is packed with one side against the side chain of Phe157, the plane of which is slightly tilted relative to the quinoxaline, and sandwiched in this position through a π-electron stacking interaction with the coplanar NAM moiety of carba-NAD^+. The interaction with Phe157 is established through a reorientation of this residue upon SRT1720 binding (Figs. 2*h* and 2*i*), enabled by a major shift of this cofactor-binding loop region to a new conformation clearly defined by electron density (Supplementary Fig. 1[1]). The conformations of other hSirt3 regions and of the co-substrate analogue carba-NAD^+ remain largely unchanged upon SRT1720 binding (Figs. 2*h* and 2*i*; see also below).

3.3. NAD^+ co-substrate and the hSirt3 cofactor-binding loop assist in the binding of SRT1720

In the hSirt3–carba-NAD^+–SRT1720 complex structure, the quinoxaline ring of the inhibitor is tightly packed between Phe157 and the NAM moiety of carba-NAD^+, with minimal distances of 3.1 and 3.0 Å, respectively, between the nearly coplanar interaction partners. This arrangement indicates that the NAM moiety of NAD^+ supports SRT1720 binding, which would explain the uncompetitive inhibition behaviour (Jin, Galonek *et al.*, 2009). Cooperative binding of NAD^+ and

[1] Supplementary material has been deposited in the IUCr electronic archive (Reference: WD5219). Services for accessing this material are described at the back of the journal.

SRT1720 is also supported by measurements of the stability of hSirt3 towards thermal denaturation, which often increases on the binding of ligands. In the presence of 50 μ*M* SRT1720, the half-point of the hSirt3 melting transition (T_m) increased to more than 326 K from less than 324 K for a DMSO control (Fig. 3*a*; Supplementary Fig. 2). Adding SRT1720 in the presence of 500 μ*M* NAD^+ further increased the T_m to above 327 K, which is consistent with NAD^+ making a positive contribution to SRT1720 binding. To further analyze the interaction between SRT1720 and NAD^+, we performed affinity measurements using microscale thermophoresis. The K_d for SRT1720 binding to hSirt3 decreased from 7.5 ± 1.3 μ*M* for the apoenzyme to 2.6 ± 0.3 μ*M* in the presence of 500 μ*M* NAD^+ (Fig. 3*b*), which is consistent with the melting experiments and uncompetitive inhibition. Providing 500 μ*M* ADP-ribose instead, which comprises most of the co-substrate NAD^+ but lacks the NAM portion, had no effect on the compound affinity (K_d = 7.8 ± 1.3 μ*M*). This result confirms the conclusion from our crystal structure analysis that NAD^+ supports binding of SRT1720 to hSirt3 by providing its NAM moiety as an interaction surface and binding-site lid.

The sirtuin cofactor-binding loop dynamically adopts different conformations during catalysis (Moniot *et al.*, 2012): NAM release and intermediate formation induce closure of the loop, thereby moving the conserved phenylalanine (Phe157 in Sirt3) towards the alkylimidate to shield against NAM and solvent. Comparison of the hSirt3–carba-NAD^+–SRT1720 complex with our Sirt3–ADP-ribose structure (Fig. 3*c*) and with an hSirt3–ACS2-peptide–carba-NAD^+ complex (Figs. 2*h* and 2*i*) shows that the binding mode of SRT1720 leads to a drastic displacement and a unique arrangement of the cofactor-binding loop region preceding helix α3, starting at Pro155. The maximal C^α shift of about 6.1 Å (compared with the hSirt3–ACS2-peptide–carba-NAD^+ complex; Fig. 2*i*) or 4.7 Å (compared with the hSirt3–ADP-ribose complex; Fig. 3*c*) is observed for Phe157, which is well inside the active centre in the hSirt3–carba-NAD^+–SRT1720 complex and forms part of the inhibitor-binding interface (see above). This significant rearrangement is only accompanied by small shifts in the loop regions C-terminal to α3 and between β6 and α10, making the large Phe157 rearrangement a locally restricted adjustment for accommodation of the compound (Fig. 2*h*). Formation of the unique loop conformation around Phe157 appears to mainly be driven by the tight packing of the π-electron systems of this protein residue,

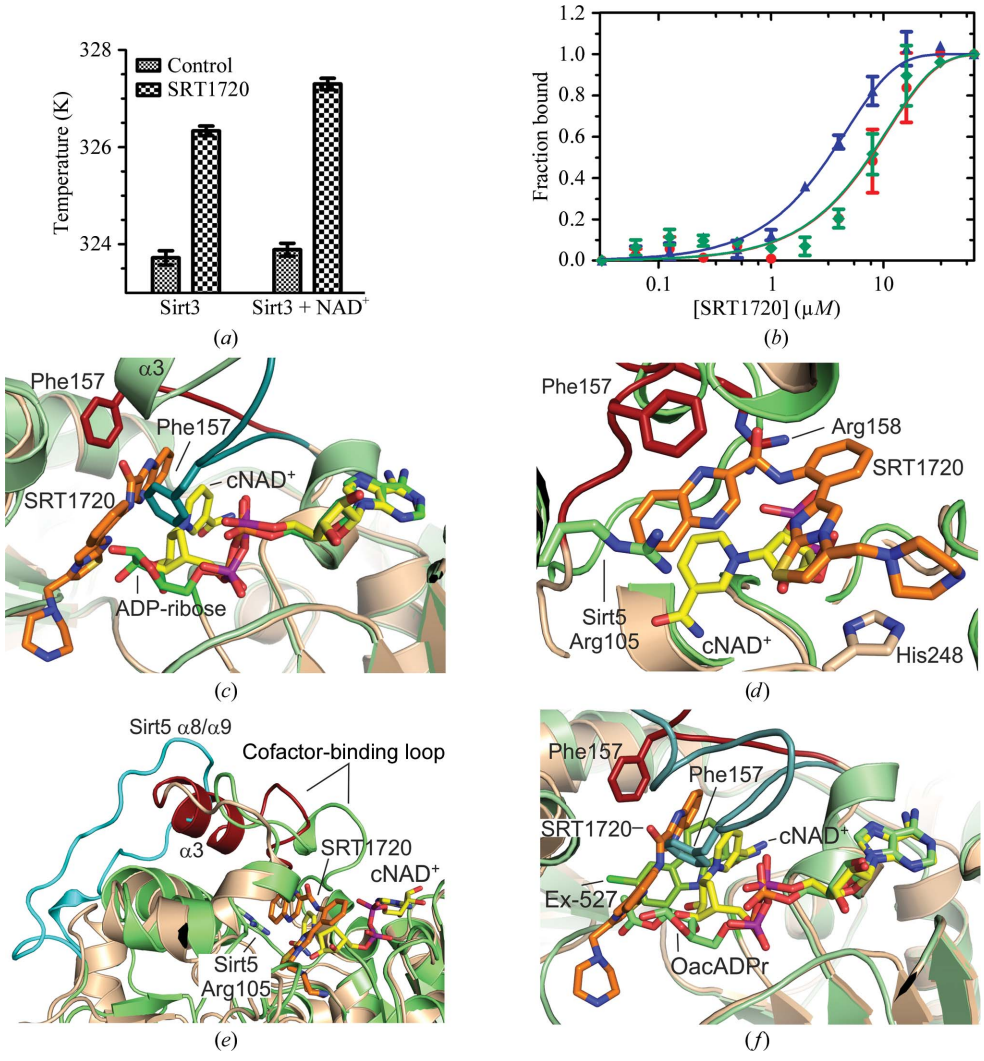

Figure 3
Analysis of the carba-NAD^+–SRT1720 interaction and comparison of the hSirt3–carba-NAD^+–SRT1720 complex with other sirtuin–inhibitor complex structures. (*a*) Melting temperatures for hSirt3 in thermal denaturation assays performed in the presence and absence of 50 μ*M* SRT1720 and 500 μ*M* NAD^+. Error bars represent standard errors of nonlinear fits. (*b*) Thermophoresis binding experiments to determine the affinity of SRT1720 for apo hSirt3 (red circles) and for hSirt3 in the presence of 500 μ*M* NAD^+ (blue triangles) or ADP-ribose (green diamonds), respectively. Error bars represent the standard errors of two independent measurements. (*c*) Comparison of the cofactor-binding loop in hSirt3–carba-NAD^+–SRT1720 (brown/red/yellow/orange) and hSirt3–ADP-ribose (green). (*d*, *e*) Comparison of hSirt3–carba-NAD^+–SRT1720 (brown/red/yellow/orange) with a Sirt5–Succ-IDH2-peptide–carba-NAD^+ complex (green, cyan; PDB entry 4g1c; Szczepankiewicz *et al.*, 2012; ligands not shown for clarity). The close-up (*d*) shows the proximity of Sirt5 Arg105 to the SRT1720 binding site in Sirt3 and (*e*) shows the Sirt5-specific extended loop (cyan) overlapping with Sirt3 α3. (*f*) Comparison of the SRT1720 binding site in hSirt3 (brown/red/yellow/orange) with the binding of Ex-527 to an hSirt3–2′-*O*-acetylated ADP-ribose complex (green). Carba-NAD^+ is labelled $cNAD^+$ and 2′-*O*-acetylated ADP-ribose is labelled OacADPr.

the inhibitor quinoxaline and the co-substrate NAM moiety. This loop conformation and sandwich-like interaction seem to stabilize the sirtuin–inhibitor complex, as indicated by the denaturation and binding experiments (see above), and the inhibitor itself thus appears to exploit the adaptability of the cofactor-binding loop to induce a target conformation favourable for its binding. The inability to form this π-electron sandwich with Sirt3–ADP-ribose should be the major reason why no inhibitor was bound to this complex crystallized in the presence of SRT1720 (see §3.1).

3.4. Isoform specificity and comparison with other sirtuin–inhibitor complexes

Different effects have been reported for SRT1720 with human sirtuin isoforms. In contrast to the potent inhibition observed for Sirt3 (Jin, Galonek *et al.*, 2009, and this study), Sirt2 and Sirt5 are only very weakly inhibited (Milne *et al.*, 2007; Suenkel *et al.*, 2013). SRT1720 was reported to not affect the activity of Sirt1 in one study (Lakshminarasimhan, Curth *et al.*, 2013) and even to activate it in another test (Milne *et al.*, 2007; see §4). An overlay of the hSirt3–carba-NAD$^+$–SRT1720 complex structure with a Sirt5–Succ-IDH2-peptide–carba-NAD$^+$ structure (Szczepankiewicz *et al.*, 2012) reveals that a Sirt5-specific residue, Arg105, would clash with SRT1720 binding (Fig. 3*d*). This residue mediates the unique specificity of Sirt5 for succinyl-Lys rather than acetyl-Lys substrates and appears to be able to sterically interfere with an inhibitory rebinding of nicotinamide to the C-site (Du *et al.*, 2011; Fischer *et al.*, 2012), and it is likely to cause the insensitivity of this isoform to SRT1720. A second factor that might contribute is the Sirt5-specific large α8/9 loop, which is packed on top of the Sirt5 region corresponding to α3 and overlaps with this Sirt3 helix, which could indicate that the corresponding Sirt5 region cannot assume the local conformation required for SRT1720 binding (Fig. 3*e*). Sirt1 might similarly have a structural element packed on top of α3, since the C-terminus of the catalytic domain (where the structurally characterized construct ends) is located in this area (Zhao *et al.*, 2013). Other subtle differences might also contribute to the isoform-specific effects, since obvious differences of Sirt1, and also the SRT1720-insensitive Sirt2 (Moniot *et al.*, 2013), from Sirt3 in the immediate vicinity of the compound are lacking. However, the Sirt1 and Sirt2 sequences start to differ two and three residues, respectively, C-terminal to the SRT1720-binding hSirt3 residues Phe157-Arg158, which is likely to influence the ability of this region to undergo the dramatic rearrangement required for SRT1720 binding. We assume that such indirect effects contribute significantly to the SRT1720 isoform selectivity.

The identified hSirt3 binding site for SRT1720 is next to the C-pocket of the enzyme, which accommodates the co-substrate NAM moiety. The C-pocket can be exploited by free NAM for inhibition and recent crystal structures of complexes of hSirt3 with pharmacological inhibitors [Ex-527 (Gertz *et al.*, 2013) and ELT-11c (Encoded Library Technology 11c; Disch *et al.*, 2013)] revealed that these compounds also occupy part of the C-site and neighbouring areas. However, these compounds use different neighbouring areas. A series of sirtuin inhibitors represented by ELT-11c and chemically related in parts to SRT1720 have recently been shown to partially resemble SRT1720 binding by occupying the acetyl-Lys binding channel, consistent with this partial chemical similarity. In contrast to SRT1720, however, these compounds inhibit sirtuins without any isoform selectivity in an NAD$^+$-competitive manner by blocking the C-site and ribose-binding pocket (Disch *et al.*, 2013). Ex-527, in contrast, shows pronounced isoform selectivity and binds to a hydrophobic pocket that partially overlaps with the binding site for the central parts of SRT1720 (Fig. 3*f*). This pocket is almost identical in most sirtuins, but the compound only binds efficiently in the presence of the 2′-*O*-acetyl-ADP-ribose product and kinetic isoform differences appear to cause the observed selectivity (Gertz *et al.*, 2013). Our comparison thus shows that SRT1720 uses a novel mode of isoform-selective inhibitor binding to a sirtuin exploiting the co-substrate NAD$^+$ in its productive conformation and an as yet unknown arrangement of the cofactor-binding loop. These findings allow a rationalization of the available activity data and provide structural information that can be exploited for further drug development.

4. Discussion and conclusions

Sirtuins are generally considered attractive targets for therapy of metabolic and aging-related diseases (Haigis & Sinclair, 2010; Lavu *et al.*, 2008). Sirt3 provides the major deacetylase activity in mitochondria, regulating a variety of pathways in metabolism and stress responses (Verdin *et al.*, 2010; Gertz & Steegborn, 2010), and it appears to be a suitable target for treating metabolic syndrome and several types of cancer (Hirschey *et al.*, 2011; Finley & Haigis, 2012). However, SRT1720 is still the only available Sirt3 inhibitor with high potency and significant isoform selectivity, and the lack of knowledge of the details of its binding site and inhibition mechanism has hampered its improvement. Our hSirt3–carba-NAD$^+$–SRT1720 structure now reveals the molecular inhibition mechanism of the compound, rationalizing its uncompetitive inhibition behaviour with NAD$^+$ (Jin, Galonek *et al.*, 2009), and provides an excellent basis for drug development. The compound blocks part of the acetyl-Lys binding site, explaining its competition with the polypeptide substrate, and forms a tightly packed π-stacking sandwich with Phe157 and NAD$^+$. The complex structure indicates several potential approaches for compound improvement. The size of the π-stacking quinoxaline ring appears to not yet be optimal, for example, and adding the missing interaction functionality for hSirt3 Glu177 to the central phenyl ring of SRT1720 should further increase the inhibitor affinity. Furthermore, introducing more polar groups in the extension at the thiazole ring could establish a hydrogen bond to the catalytic His (His248 in hSirt3) and should also improve the poor solubility of the compound.

SRT1720 was initially identified as a Sirt1 activator with improved potency compared with resveratrol (Milne *et al.*,

2007), but these activating effects have been questioned (Pacholec *et al.*, 2010). We were initially unable to activate Sirt1 with SRT1720 using the fluorophor-labelled 'Fluor-de-Lys-1' (FdL-1) peptide (Lakshminarasimhan, Curth *et al.*, 2013). However, through changing the assay conditions, in particular by increasing the substrate concentrations fourfold (to 0.1 m*M* peptide and 1 m*M* NAD^+), we could activate Sirt1, while Sirt2 was unaffected and Sirt3 was inhibited (Supplementary Fig. S3), confirming that compounds can have opposite effects on different isoforms (Milne *et al.*, 2007; Gertz *et al.*, 2012). No Sirt1 activation was reported with unlabelled p53 peptide substrate (Pacholec *et al.*, 2010), but recent work has shown that Sirt1 can be activated against nonlabelled substrates and that the effect depends on the substrate sequence (Hubbard *et al.*, 2013; Lakshminarasimhan, Rauh *et al.*, 2013). An activation mechanism through a substrate–compound contact in the sirtuin–substrate–activator complex was proposed based on a Sirt5–FdL-1–resveratrol complex structure (Gertz *et al.*, 2012). This binding site does not explain the available structure–activity relationships well (Milne *et al.*, 2007; Vu *et al.*, 2009), however, and an alternative mechanism could be based on an allosteric site, as indicated by structural studies with a halogenated resveratrol (Nguyen, unpublished work). Nevertheless, it is tempting to speculate whether the observed SRT1720 binding mode might also explain the Sirt1 activation. A Sirt1 state after intermediate formation that is able to release deacetylated peptide upon activator binding would have to be an SRT1720 acceptor to avoid inhibition through peptide competition. Sirtuin inhibition by Ex-527 is based on compound binding to a product complex (Gertz *et al.*, 2013), and we thus speculate that SRT1720 binding after product formation could activate Sirt1 by promoting product release, a potentially rate-limiting step in sirtuin catalysis (Borra *et al.*, 2004; Gertz *et al.*, 2013), since SRT1720 would clash with the acetyl-ribose group of the co-product (Figs. 3*c* and 3*e*). However, further studies will be required to confirm Sirt1 activation by SRT1720 and other compounds towards physiological substrates and to fully clarify the activation mechanisms of the compounds.

Our hSirt3–carba-NAD^+–SRT1720 structure unequivocally reveals the mechanism of hSirt3 inhibition and shows that the NAM moiety and cofactor-binding loop geometry are important for efficient SRT1720 binding. The cofactor-binding loop, besides adapting to different states of the co-substrate during catalysis (Moniot *et al.*, 2012), can also respond to additional ligands, as impressively demonstrated by the previously unobserved loop conformation arranging Phe157 for SRT1720 binding. The structure thus not only provides structural information for the improvement of SRT1720 and related compounds, but also provides a novel binding site and template conformation for docking screens or structure-assisted drug design. The other structurally characterized Sirt3 inhibitors block the NAM-binding site (Disch *et al.*, 2013; Gertz *et al.*, 2013), but our comparison suggests different subgroups for these 'extended C-site' (ECS) inhibitors (Gertz *et al.*, 2013) based on the pocket extension used by Ex-527 (group I) and ELT-11c (group II). SRT1720 shares acetyl-Lys pocket binding with ELT-11c but uses an alternative binding mode for inhibition with NAM in the C-site. Combining binding mode and groups of SRT1720 with moieties, for example, exploiting the Ex-527 extension opens new opportunities for the development of sirtuin-targeting drugs. Our results thus provide a novel mechanism and target conformation for Sirt3 inhibition and reveal detailed structural information for aiding the development of improved sirtuin-targeting drugs.

We are very grateful to Georg Vlasuk and Bruce Szczepankiewicz (Sirtris, a GSK company) for providing us with carba-NAD^+. We thank Norbert Grillenbeck, Paul Gehrtz, the UBT synchrotron teams and the beamline staff of BESSY MX14.1 (Helmholtz-Zentrum Berlin) for technical assistance. This work was supported through grant STE1701/5 from Deutsche Forschungsgemeinschaft (CS) and Elite Network Bavaria (GN, CS).

References

Avalos, J. L., Boeke, J. D. & Wolberger, C. (2004). *Mol. Cell*, **13**, 639–648.
Borra, M. T., Langer, M. R., Slama, J. T. & Denu, J. M. (2004). *Biochemistry*, **43**, 9877–9887.
Cen, Y. (2010). *Biochim. Biophys. Acta*, **1804**, 1635–1644.
Chang, J.-H., Kim, H.-C., Hwang, K.-Y., Lee, J.-W., Jackson, S. P., Bell, S. D. & Cho, Y. (2002). *J. Biol. Chem.* **277**, 34489–34498.
Chen, L. (2011). *Curr. Med. Chem.* **18**, 1936–1946.
Chen, V. B., Arendall, W. B., Headd, J. J., Keedy, D. A., Immormino, R. M., Kapral, G. J., Murray, L. W., Richardson, J. S. & Richardson, D. C. (2010). *Acta Cryst.* D**66**, 12–21.
Cheng, Y. & Prusoff, W. H. (1973). *Biochem. Pharmacol.* **22**, 3099–3108.
Disch, J. S. *et al.* (2013). *J. Med. Chem.* **56**, 3666–3679.
Du, J. *et al.* (2011). *Science*, **334**, 806–809.
Emsley, P. & Cowtan, K. (2004). *Acta Cryst.* D**60**, 2126–2132.
Finley, L. W. & Haigis, M. C. (2012). *Trends Mol. Med.* **18**, 516–523.
Fischer, F., Gertz, M., Suenkel, B., Lakshminarasimhan, M., Schutkowski, M. & Steegborn, C. (2012). *PLoS One*, **7**, e45098.
Gertz, M., Fischer, F., Nguyen, G. T. T., Lakshminarasimhan, M., Schutkowski, M., Weyand, M. & Steegborn, C. (2013). *Proc. Natl Acad. Sci.* doi: 10.1073/pnas.1303628110.
Gertz, M., Nguyen, G. T. T., Fischer, F., Suenkel, B., Schlicker, C., Fränzel, B., Tomaschewski, J., Aladini, F., Becker, C., Wolters, D. & Steegborn, C. (2012). *PLoS One*, **7**, e49761.
Gertz, M. & Steegborn, C. (2010). *Biochim. Biophys. Acta*, **1804**, 1658–1665.
Haigis, M. C. & Sinclair, D. A. (2010). *Annu. Rev. Pathol.* **5**, 253–295.
Hirschey, M. D. *et al.* (2011). *Mol. Cell*, **44**, 177–190.
Hoff, K. G., Avalos, J. L., Sens, K. & Wolberger, C. (2006). *Structure*, **14**, 1231–1240.
Hubbard, B. P. *et al.* (2013). *Science*, **339**, 1216–1219.
Jin, L., Galonek, H. *et al.* (2009). *Protein Sci.* **18**, 514–525.
Jin, L., Wei, W., Jiang, Y., Peng, H., Cai, J., Mao, C., Dai, H., Choy, W., Bemis, J. E., Jirousek, M. R., Milne, J. C., Westphal, C. H. & Perni, R. B. (2009). *J. Biol. Chem.* **284**, 24394–24405.
Kabsch, W. (2010). *Acta Cryst.* D**66**, 125–132.
Karplus, P. A. & Diederichs, K. (2012). *Science*, **336**, 1030–1033.
Kleywegt, G. J. (1999). *Acta Cryst.* D**55**, 1878–1884.
Kleywegt, G. J. (2000). *Acta Cryst.* D**56**, 249–265.
Lakshminarasimhan, M., Curth, U., Moniot, S., Mosalaganti, S., Raunser, S. & Steegborn, C. (2013). *Biosci. Rep.* **33**, e00037.
Lakshminarasimhan, M., Rauh, D., Schutkowski, M. & Steegborn, C. (2013). *Aging*, **5**, 151–154.

Laskowski, R. A., Moss, D. S. & Thornton, J. M. (1993). *J. Mol. Biol.* **231**, 1049–1067.
Laurent, G. *et al.* (2013). *Mol Cell*, **50**, 686–698.
Lavu, S., Boss, O., Elliott, P. J. & Lambert, P. D. (2008). *Nature Rev. Drug Discov.* **7**, 841–853.
Michan, S. & Sinclair, D. (2007). *Biochem. J.* **404**, 1–13.
Milne, J. C. *et al.* (2007). *Nature (London)*, **450**, 712–716.
Minor, R. K., Allard, J. S., Younts, C. M., Ward, T. M. & de Cabo, R. (2010). *J. Gerontol. A Biol. Sci. Med. Sci.* **65**, 695–703.
Moniot, S., Schutkowski, M. & Steegborn, C. (2013). *J. Struct. Biol.* **182**, 136–143.
Moniot, S., Weyand, M. & Steegborn, C. (2012). *Front. Pharmacol.* **3**, 16.
Mueller, U., Darowski, N., Fuchs, M. R., Förster, R., Hellmig, M., Paithankar, K. S., Pühringer, S., Steffien, M., Zocher, G. & Weiss, M. S. (2012). *J. Synchrotron Rad.* **19**, 442–449.
Murshudov, G. N., Skubák, P., Lebedev, A. A., Pannu, N. S., Steiner, R. A., Nicholls, R. A., Winn, M. D., Long, F. & Vagin, A. A. (2011). *Acta Cryst.* D**67**, 355–367.
North, B. J., Marshall, B. L., Borra, M. T., Denu, J. M. & Verdin, E. (2003). *Mol. Cell*, **11**, 437–444.
Pacholec, M. *et al.* (2010). *J. Biol. Chem.* **285**, 8340–8351.
Sanders, B. D., Jackson, B. & Marmorstein, R. (2010). *Biochim. Biophys. Acta*, **1804**, 1604–1616.
Sauve, A. A., Wolberger, C., Schramm, V. L. & Boeke, J. D. (2006). *Annu. Rev. Biochem.* **75**, 435–465.
Schlicker, C., Boanca, G., Lakshminarasimhan, M. & Steegborn, C. (2011). *Aging*, **3**, 852–857.
Schüttelkopf, A. W. & van Aalten, D. M. F. (2004). *Acta Cryst.* D**60**, 1355–1363.
Suenkel, B., Fischer, F. & Steegborn, C. (2013). *Bioorg. Med. Chem. Lett.* **23**, 143–146.
Szczepankiewicz, B. G., Dai, H., Koppetsch, K. J., Qian, D., Jiang, F., Mao, C. & Perni, R. B. (2012). *J. Org. Chem.* **77**, 7319–7329.
Verdin, E., Hirschey, M. D., Finley, L. W. & Haigis, M. C. (2010). *Trends Biochem. Sci.* **35**, 669–675.
Vu, C. B. *et al.* (2009). *J. Med. Chem.* **52**, 1275–1283.
Wallace, A. C., Laskowski, R. A. & Thornton, J. M. (1995). *Protein Eng.* **8**, 127–134.
Wienken, C. J., Baaske, P., Rothbauer, U., Braun, D. & Duhr, S. (2010). *Nature Commun.* **1**, 100.
Zhao, X., Allison, D., Condon, B., Zhang, F., Gheyi, T., Zhang, A., Ashok, S., Russell, M., MacEwan, I., Qian, Y., Jamison, J. A. & Luz, J. G. (2013). *J. Med. Chem.* **56**, 963–969.